Pressure-induced topological insulator-to-metal transition and superconductivity in Sn-doped Bi_{1.1}Sb_{0.9}Te_{2}S

Chao An, Xuliang Chen, Bin Wu, Yonghui Zhou, Ying Zhou, Ranran Zhang, Changyong Park, Fengqi Song, and Zhaorong Yang

Phys. Rev. B **97**, 174516 — Published 21 May 2018

DOI: 10.1103/PhysRevB.97.174516

Pressure-induced topological insulator-to-metal transition and superconductivity in Sn-doped $Bi_{1.1}Sb_{0.9}Te_2S$

Chao An[1,2], Xuliang Chen[1,*], Bin Wu[3], Yonghui Zhou[1], Ying Zhou[1], Ranran Zhang[1], Changyong Park[4], Fengqi Song[3,6], Zhaorong Yang[1,5,6,*]

[1]*Anhui Province Key Laboratory of Condensed Matter Physics at Extreme Conditions, High Magnetic Field Laboratory, Chinese Academy of Sciences, Hefei 230031, China*

[2]*University of Science and Technology of China, Hefei 230026, China*

[3]*National Laboratory of Solid State Microstructures, School of Physics, Nanjing University, Nanjing 210093, China*

[4]*HPCAT, Geophysical Laboratory, Carnegie Institution of Washington, Argonne 60439, USA*

[5]*Institute of Physical Science and Information Technology, Anhui University, Hefei 230601, China*

[6]*Collaborative Innovation Center of Advanced Microstructures, Nanjing 210093, China*

*Corresponding authors. E-mails: xlchen@hmfl.ac.cn; zryang@issp.ac.cn

Tetradymite-type topological insulator (TI) Sn-doped $Bi_{1.1}Sb_{0.9}Te_2S$ (Sn-BSTS), with a surface state Dirac point energy well isolated from the bulk valence and conduction bands, is an ideal platform for studying the topological transport phenomena. Here, we present high-pressure transport studies on single crystal Sn-BSTS, combined with Raman scattering and synchrotron x-ray diffraction measurements. Over the studied pressure range of 0.7-37.2 GPa, three critical pressure points can be observed: (i) at ~9 GPa, a pressure-induced topological insulator-to metal transition is revealed due to closure of the bulk bandgap, which is accompanied by changes in slope of the Raman frequencies and a minimum in *c/a* within the pristine rhombohedral structure (*R-3m*); (ii) at ~13 GPa, superconductivity is observed to emerge, along with the *R-3m* to a *C2/c* (monoclinic) structural transition; (iii) at ~24 GPa, the superconducting transition onset temperature T_C reaches a maximum of ~12 K, accompanied by a second structural transition from the *C2/c* to a body centered cubic *Im-3m* phase.

I. INTRODUCTION

Pressure tuning of structural and electrical properties in tetradymite-type topological insulators (TIs) like Bi_2Se_3, Bi_2Te_3 and Sb_2Te_3 have attracted much attention because of discoveries of a variety of interesting phenomena [1-22]. For instance, synchrotron x-ray diffraction and Raman scattering measurements in Bi_2Se_3 reveal a minimum in the lattice parameters ratio *c/a* and changes in pressure dependences of the Raman frequencies at the same low pressure far before a structural phase transition [1]; meanwhile, discontinuities in conductivity are observed around this critical pressure [2]. Similar situations are also encountered in other members of tetradymite-type TIs [3-10], despite that the critical pressures are somewhat different. Due to the absence of a structural transition, these anomalies were usually related to a pressure-induced electronic topological transition (ETT) or Lifshitz transition. As is known, the Lifshitz transition [23] links to the van Hove singularity associated with the band extrema passing through the Fermi level, and in the presence of such transition the distribution of carriers and Fermi surface topology changes. Considering the lack of such changes, Bera *et al.* [11] thus termed the transition as an isostructural transition, instead of the ETT. Obviously, the origins of these anomalies still remain elusive. Besides, superconductivity is commonly observed in these TIs at high pressures [12-17]. Interest is widely sparked by the expectation of realizing topological superconductivity [16], in spite of the absence of direct experimental evidences so far.

TI is characterized by the insulating bulk state and metallic topological surface states (TSSs) that are protected by time reversal symmetry. Ideally, a surface state Dirac point energy is isolated well from the bulk valence and conduction bands. Experimentally, for as-grown tetradymite-type nominally stoichiometric TIs, a metallic bulk conduction arising from inherent Se/Te deficiencies usually overwhelms the surface transport [24-26]. Therefore, it is hard to unveil the pressure evolutions of the intrinsic conductions of the bulk insulating state and TSSs via transport, which in

turn may result in misunderstanding of the structural responses to external pressure.

In view of the above, here we present a systematic study of the electrical, structural and vibrational properties on a recently discovered TI Sn-doped $Bi_{1.1}Sb_{0.9}Te_2S$ (Sn-BSTS) [27] in diamond anvil cells with pressures up to 37.2 GPa, which has a well-isolated bulk state from the TSSs. Thanks to such unique band structure of Sn-BSTS, we can successfully trace the pressure evolutions of the bulk and TSSs conductivities separately, which are vital for unveiling the topological insulator-to-metal transition-related structural and vibrational anomalies, instead of an ETT. Interestingly, the T_C-maximum of ~12 K obtained here is the highest value among all the pressurized tetradymite-type TIs.

II. EXPERIMENTAL DETAILS

Sn-BSTS single crystals were grown by modified Bridgman technique [28]. The high quality of the single crystals was checked by single crystal and powder x-ray diffractions as well as energy dispersive spectra (see Fig. S1 and notes in the Supplemental Material for more details) [29]. Standard four-probe method was employed to perform the high-pressure electrical transport measurements in a temperature range of 1.8-300 K in a Be-Cu diamond anvil cell (DAC), designed by the Honest Machinery Designer's office (HMD), Japan. A piece of single crystal cleaved from the bulk Sn-BSTS single crystal was loaded with sodium chloride (NaCl) powder as the pressure transmitting medium and the current was introduced in the *ab* plane.

Pressure was generated by Mao-Bell type symmetric DAC for the synchrotron x-ray diffraction (XRD) and Raman scattering measurements. Raman scattering measurements were performed at room temperature on freshly cleaved Sn-BSTS single crystals using 532-nm solid-state laser for excitation with the power below 1% to avoid sample damage and any heating effect, at the Center for High Pressure Science and Technology Advanced Research (HPSTAR) in Shanghai. Neon was used

as the pressure transmitting medium. We also repeated our high-pressure Raman measurements at the China High Magnetic Field Laboratory (CHMFL) in Hefei using Daphne 7373 as the pressure medium. High pressure synchrotron powder XRD (λ = 0.4133 Å) was performed at room temperature at the beamline of 16 BM-D, HPCAT [30] of Advanced Photon Source, Argonne National Laboratory. Daphne 7373 was used as the pressure transmitting medium. The DIOPTAS [31] program was used for image integrations and Le Bail method was employed to fit the XRD data with the RIETICA [32] program. Ruby fluorescence method [33] was used to determine the pressure for all of the above experiments.

III. RESULTS AND DISCUSSION

Figure 1(a) displays the temperature (T) dependence of the electrical resistance (R) of the Sn-BSTS single crystal at pressures from 0.7 to 10.5 GPa. At 0.7 GPa, a huge resistance hump at T_h ~170 K is observed, in agreement with that measured at ambient pressure [27]. At ambient pressure, the conductance of Sn-BSTS is considered as a sum of two parallel channels: surface (σ_S) and bulk (σ_B) conductances [34]. For simplicity, a two-channel model with the formula of $\sigma(T)=\sigma_S(T)+\sigma_B(T)$ is employed. The former contribution is written as $\sigma_S(T)=1/\rho_S(T)$, where $\rho_S(T)=\rho_0+bT^2+cT$, while the latter one is expressed as $\sigma_B(T)=1/\rho_B(T)$, where $\rho_B(T)=a\exp(E_g/2k_BT)$ [35]. Figure 1(b) shows the fitting results with the two-channel model at 0.7 GPa, in which the dashed and solid lines represent σ_S and σ_B, respectively. It yields a bulk bandgap E_g = 294 meV, which is a little smaller than 350 meV revealed by ARPES for Sn-BSTS at ambient pressure [27]. Upon compression to 3.8 GPa, the T_h shifts towards lower temperatures rapidly, which indicates that the contribution of the bulk state to the total conductivity becomes increasingly dominant. As displayed in Fig. 1(c), the conductivity of the bulk

state shows a rapid enhancement with increasing pressure, while that of the surface state increases marginally upon compression. At 6.4 GPa, the resistance exhibits a semiconducting-like behavior in the whole temperature range, suggesting that the contribution of topological surface states (TSSs) are overwhelmed by that of the bulk state. Further increasing the pressure to 10.5 GPa, a partial metallic behavior below 190 K is observed, signaling the metallization of the bulk state.

As the contribution of the TSSs can also be identified through magnetotransport measurements, magnetoresistance (*MR*) was measured at 5 K under various pressures up to 10.5 GPa with magnetic fields perpendicular to the *ab* plane, as shown in Fig. 1(d). One can see that the *MR* decreases monotonically with increasing pressure. In the low pressure region of 0.7-3.8 GPa, *MR* exhibits a concave behavior, which is very similar to that observed in the tetradymite-type TIs and can be attributed to weak antilocalization originating from the TSSs [36, 37]. Further increasing the pressure, the *MR* changes to a convex behavior at 6.4 GPa, above which a classical power-law behavior ($MR \propto H^2$) develops gradually. These observations indicate that the bulk state conductance dominates above 6.4 GPa, in excellent consistent with the results from the *R-T* data shown in Fig. 1(a).

Upon further compression to 12.6 GPa, a pronounced resistance drop is clearly seen below ~4 K as presented in Figs. 2(a) and 2(b). Zero resistance is observed at 14.3 GPa, suggesting the appearance of superconductivity in the pressurized Sn-BSTS. The presence of superconductivity is further confirmed by the temperature dependence of resistance measurements under various magnetic fields perpendicular to the *ab* plane at 14.3 GPa. As shown in Fig. 2(c), the superconducting transition temperature T_C is monotonically decreased with increasing magnetic field and the resistance drop is almost smeared out at 1.5 T. The inset of Fig. 2(c) shows the upper critical field $\mu_0 H_{C2}$ as a function of temperature. Here the $\mu_0 H_{C2}$ value is defined from the resistance criterion of R_{cri} = 90% R_n (R_n is the normal state resistance near T_C). The upper critical field $\mu_0 H_{C2}$ is estimated to be 2.31 T according to the

Werthamer-Helfand-Hohenberg (WHH) equation [38].

To check the relationship between superconductivity and structure, *in situ* high-pressure synchrotron XRD measurements were performed on powdered single crystal Sn-BSTS up to 31.6 GPa. The experimental patterns are presented in Fig. 3(a). Upon compression, the rhombohedral structure (*R-3m*) of Sn-BSTS is found to be stable up to 11.7 GPa, above which several new peaks show up as denoted by arrows, suggesting occurrence of a structural transition. In the intermediate pressure range, this new structural phase is observed to coexist with the low-pressure pristine one. With increasing pressure above 19.1 GPa, the low-pressure *R-3m* phase disappears completely, while another new structural phase transition takes place, as indicated by appearance of new peaks. Both high pressure phases coexists up to the highest pressure of 31.6 GPa achieved in the present study. We also plot the phase quantification as a function of pressure in Fig. S2. In addition to two critical pressures relating to the structural phase transition, phase coexistences and their respective evolutions with pressure are also clearly revealed. After carefully analyzing and fitting the data, we found that the pressure-induced structural transition sequence in Sn-BSTS is *R-3m*→*C2/c*→*Im-3m*, in agreement with those observed in its brother compounds Bi_2Te_3 and Sb_2Te_3 [18-20]. Typical standard Rietveld refinements at 1.3, 15.0 and 31.6 GPa are displayed in Fig. 3(b). The corresponding fit parameters are displayed in TABLE S1.

The detailed lattice parameters and volume as a function of pressure are exhibited in Figs. 3(c) and 3(d). The equation of state (EoS) was fitted by using the third-order Birch-Murnaghan formula [39]:

$$P = \frac{3}{2} B_0 [(V_0 / V)^{\frac{7}{3}} - (V_0 / V)^{\frac{5}{3}}] \{1 + \frac{3}{4}(B_0^{'} - 4)[(V_0 / V)^{\frac{2}{3}} - 1]\}, \quad (1)$$

where V_0, B_0 and $B_0^{'}$ are the volume, bulk modulus $-V/(dV/dP)$, and first order derivative of the bulk modulus at zero pressure, respectively. The fitting yields V_0 = 153.7 Å^3, B_0 = 51.4 GPa, and $B_0^{'}$ = 7.0 for *R-3m* phase; 141.7 Å^3, 97.2 GPa

and 7.4 for *C2/c* phase; and 137.5 Å^3, 122.9 GPa and 4.0 for *Im-3m* phase. In addition, the volume collapses at these two structural transition pressures are estimated to be about 1.8% and 3.0%, respectively, indicating both structural transitions are first order.

The structural transitions are also reflected in Raman measurements as shown in Fig. 4. At 1.3 GPa, two main peaks centered at 112.7 and 170.4 cm^{-1} are observed, similar to those observed at ambient pressure [Fig. S1(d) and Ref. 27]. These two peaks can be assigned to the E_g and A_{2g} vibrational modes [27], respectively. With increasing pressure, both Raman peaks move towards higher frequencies monotonically. At 12.6 GPa, a new peak at 156.8 cm^{-1} develops due to the structural transition from *R-3m* to *C2/c*, which can be assigned to the A_g mode [4, 6]. Upon further compression above 24.2 GPa, all Raman mode disappears relating to the structural transition from *C2/c* to *Im-3m*. These conclusions are reproducible from a second high-pressure Raman experiment except for minor difference in the critical pressure values [Fig. S3].

To obtain a comprehensive understanding of the pressure-induced metallization and superconductivity in TI Sn-BSTS, the pressure dependences of the frequency and full width at half maximum (FWHM) of Raman modes, lattice parameters ratio *c/a*, bulk gap E_g and superconducting critical temperature T_C are plotted together in Fig. 5. It is found that the lattice ratio *c/a* shows a minimum around 9 GPa [Fig. 5(a)]. Concurrently, clear changes in the slope of Raman frequencies and the FWHM of the E_g and A_{2g} mode are observed [Figs. 5(b) and 5(c)]. Meanwhile, closure of the bulk gap is estimated at ~9 GPa by extrapolating the E_g vs. P curve [wine dashed line in Fig. 5(d)]. Consequently, all of these structural and vibrational anomalies at ~9 GPa should be related to the closure of the bulk gap, i.e. a pressure-induced topological insulator to metal transition, through electron-phonon coupling [40, 41].

We note that similar anomalous behaviors have been reported in previous high-pressure studies of tetradymite-type TIs, which were attributed to an electronic

topological transition (ETT) [1, 4-9]. On the one hand, to check whether there is an ETT in Sn-BSTS or not, we have plotted the reduced pressure versus Eulerian strain [5]. In Fig. S4, one can see that only linear behaviors are observed, in stark contrast to previous cases, probably indicating the absence of ETT. On the other hand, as reported previously, the transport behavior in these parent TIs is dominated by the inherent impurity states [24, 26]. The impurity states contribute a metallic transport that overwhelms the contributions from the TSSs, resulting in the experimentally observed metallic feature in *R*-*T* [24]. Therefore, the interference from the impurity states may mask the pressure effect on inherent electrical, structural and vibrational responses of both TSSs and bulk state. In the present case, due to the unique electrical band structure of TI Sn-BSTS, we can trace the pressure dependencies of the TSSs and bulk state separately. Importantly, a pressure-induced topological insulator-to-metal transition of Sn-BSTS is successfully unveiled, which is simultaneously accompanied by structural and vibrational anomalies. In view of the above two points, we argue that the previously-observed anomalies in pressurized tetradymite-type parent TIs might be related to the closure of the bulk bandgap of the topological insulator, instead of the ETT [1, 4-7].

Upon further increasing pressure, another two critical pressures can be clearly discerned relating to the successive structural transitions. Accompanied by the first structural transition, superconductivity is observed at ~13 GPa with T_C ~3.8 K. Further increasing the pressure, the FWHM of the A_g mode is observed to enhance gradually, implying an increasing electron-phonon coupling [40, 41]. Meanwhile, T_C also increases rapidly [Fig. 5(d)], probably hinting at a phonon-mediated superconductivity. T_C reaches a maximum value of ~12 K at 21.8 GPa, around which the second structural transition happens.

In the tetradymite-type TIs family [12, 15-17, 42], the occurrence of superconductivity under high pressure is commonly accompanied by a structural transition or structural instability; the T_C increases rapidly and reaches a maximum at

225 a higher pressure, where a second structural transition appears. This is also true for the
226 present case of Sn-BSTS. However, the T_C trend in the second high-pressure
227 structural phase is somewhat different. In the Se-dominated compounds, for example
228 Bi_2Se_3 [15] and $Sr_{0.065}Bi_2Se_3$ [42], T_C keeps almost constant with pressure, which was
229 considered as an indication of unconventional superconductivity; in Te-dominated
230 compounds, for example Bi_2Te_3 [12] and here Sn-BSTS, T_C decreases gradually with
231 pressure. This might be related to difference in the high-pressure structural
232 symmetries: generally a tetragonal *I4/mmm* or a BCC-like *C2/m* lattice develops for
233 the former while a cubic *Im-3m* lattice for the latter. Interestingly, the T_C-maximum
234 obtained here is the highest value in this TIs family studied so far.
235

236 **IV. CONCLUSIONS**

237 In summary, we have investigated the high-pressure electrical, structural and
238 vibrational properties of TI Sn-doped $Bi_{1.1}Sb_{0.9}Te_2S$ with pressures up to 37.2 GPa.
239 With increasing pressure, a pressure-induced metallization from closure of the bulk
240 gap is revealed around 9 GPa, accompanied by a change in slope of the Raman modes
241 and a minimum in the lattice ratio of *c/a*. Furthermore, superconductivity is observed
242 at 12.6 GPa and T_C reaches the maximum of ~12 K at 21.8 GPa, which is the highest
243 T_C ever reported in tetradymite-type TIs. Based on the synchrotron XRD and Raman
244 measurements, the appearance of superconductivity and the decrease in T_C could be
245 related to successive structural transitions.

ACKNOWLEDGEMENTS

This research was supported by the National Key Research and Development Program of China (Grant No. 2016YFA0401804), the NSFC (Grant Nos. U1632275, 11574323, 11704387), the NSF of Anhui Province (1708085QA19), the Director's Fund of Hefei Institutes of Physical Science, CAS (YZJJ201621). The x-ray work was performed at HPCAT (Sector 16), Advanced Photon Source, Argonne National Laboratory. HPCAT operations are supported by DOE-NNSA under Award No. DE-NA0001974 and DOE-BES under Award No. DE-FG02-99ER45775, with partial instrumentation funding by NSF. The Advanced Photon Source is a U.S. Department of Energy (DOE) Office of Science User Facility operated for the DOE Office of Science by Argonne National Laboratory under Contract No. DE-AC02-06CH11357. We thank Dr. Haiyun Shu for his help with gas loading and Dr. Wenge Yang for facilitating the Raman experiments at HPSTAR, Shanghai.

REFERENCE

[1] R. Vilaplana, D. Santamaría-Pérez, O. Gomis, F. J. Manjón, J. González, A. Segura, A. Muñoz, P. Rodríguez-Hernández, E. Pérez-González, V. Marín-Borrás, V. Muñoz-Sanjose, C. Drasar, and V. Kucek, Phys. Rev. B **84**, 184110 (2011).

[2] J. K. Zhang, Y. H. Han, C. L. Liu, X. Zhang, F. Ke, G. Peng, Y. M. Ma, Y. Z. Ma, and C. X. Gao, Appl. Phys. Lett. **105**, 062102 (2014).

[3] A. Nakayama, M. Einaga, Y. Tanabe, S. Nakano, F. Ishikawa, and Y. Yamada, High Pressure Res. **29**, 245 (2009).

[4] O. Gomis, R. Vilaplana, F. J. Manjón, P. Rodríguez-Hernández, E. Pérez-González, A. Muñoz, V. Kucek, and C. Drasar, Phys. Rev. B **84**, 174305 (2011).

[5] A. Polian, M. Gauthier, S. M. Souza, D. M. Trichês, J. C. de Lima, and T. A. Grandi, Phys. Rev. B **83**, 113106 (2011).

[6] R. Vilaplana, O. Gomis, F. J. Manjón, A. Segura, E. Pérez-González, P. Rodríguez-Hernández, A. Muñoz, J. González, V. Marín-Borrás, V. Muñoz-Sanjosé, C. Drasar, and V. Kucek, Phys. Rev. B **84**, 104112 (2011).

[7] G. K. Pradhan, A. Bera, P. Kumar, D. V. S. Muthu, and A. K. Sood, Solid State Commun. **152**, 284 (2012).

[8] S. M. Souza, C. M. Poffo, D. M. Trichês, J. C. de Lima, T. A. Grandi, A. Polian, and M. Gauthier, Physica B **407**, 3781 (2012).

[9] F. J. Manjón, R. Vilaplana, O. Gomis, E. Pérez-González, D. Santamaría-Pérez, V. Marín-Borrás, A. Segura, J. González, P. Rodríguez-Hernández, A. Muñoz, C. Drasar, V. Kucek, and V. Muñoz-Sanjosé, Phys. Status Solidi B **250**, 669 (2013).

[10] J. K. Zhang, C. L. Liu, X. Zhang, F. Ke, Y. H. Han, G. Peng, Y. Z. Ma, and C. X. Gao, Appl. Phys. Lett. **103**, 052102 (2013).

[11] A. Bera, K. Pal, D. V. S. Muthu, U. V. Waghmare, and A. K. Sood, J. Phys. Condens. Matter **28**, 105401 (2016).

[12] K. Matsubayashi, T. Terai, J. S. Zhou, and Y. Uwatoko, Phys. Rev. B **90**,

125126 (2014).

[13] J. Zhu, J. L. Zhang, P. P. Kong, S. J. Zhang, X. H. Yu, J. L. Zhu, Q. Q. Liu, X. Li, R. C. Yu, R. Ahuja, W. G. Yang, G. Y. Shen, H. K. Mao, H. M. Weng, X. Dai, Z. Fang, Y. S. Zhao, and C. Q. Jin, Sci. Rep. **3**, 2016 (2013).

[14] P. P. Kong, J. L. Zhang, S. J. Zhang, J. Zhu, Q. Q. Liu, R. C. Yu, Z. Fang, C. Q. Jin, W. G. Yang, X. H. Yu, J. L. Zhu, and Y. S. Zhao, J. Phys. Condens. Matter **25**, 362204 (2013).

[15] K. Kirshenbaum, P. S. Syers, A. P. Hope, N. P. Butch, J. R. Jeffries, S. T. Weir, J. J. Hamlin, M. B. Maple, Y. K. Vohra, and J. Paglione, Phys. Rev. Lett. **111**, 087001 (2013).

[16] J. L. Zhang, S. J. Zhang, H. M. Weng, W. Zhang, L. X. Yang, Q. Q. Liu, S. M. Feng, X. C. Wang, R. C. Yu, L. Z. Cao, L. Wang, W. G. Yang, H. Z. Liu, W. Y. Zhao, S. C. Zhang, X. Dai, Z. Fang, and C. Q. Jin, Proc. Natl. Acad. Sci. U.S.A. **108**, 24 (2011).

[17] C. Zhang, L. L. Sun, Z. Y. Chen, X. J. Zhou, Q. Wu, W. Yi, J. Guo, X. L. Dong, and Z. X. Zhao, Phys. Rev. B **83**, 140504(R) (2011).

[18] M. Einaga, A. Ohmura, A. Nakayama, F. Ishikawa, Y. Yamada, and S. Nakano, Phys. Rev. B **83**, 092102 (2011).

[19] J. G. Zhao, H. Z. Liu, L. Ehm, Z. Q. Chen, S. Sinogeikin, Y. S. Zhao, and G. D. Gu, Inorg. Chem. **50**, 11291 (2011).

[20] Y. M. Ma, G. T. Liu, P. W. Zhu, H. Wang, X. Wang, Q. L. Cui, J. Liu, and Y. M. Ma, J. Phys. Condens. Matter **24**, 475403 (2012).

[21] Z. H. Yu, L. Wang, Q. Y. Hu, J. G. Zhao, S. Yan, K. Yang, S. Sinogeikin, G. D. Gu, and H. K. Mao, Sci. Rep. **5**, 15939 (2015).

[22] H. Cheng, J. R. Zhang, Y. C. Li, G. Li, and X. D. Li, J. Appl. Phys. **121**, 225902 (2017).

[23] I. M. Lifshitz, Sov. Phys. JEPT **11**, 1130 (1960).

[24] J. G. Checkelsky, Y. S. Hor, M. H. Liu, D. X. Qu, R. J. Cava, and N. P. Ong, Phys. Rev. Lett. **103**, 246601 (2009).

[25] Y. L. Chen, J. G. Analytis, J. H. Chu, Z. K. Liu, S. K. Mo, X. L. Qi, H. J. Zhang, D. H. Lu, X. Dai, Z. Fang, S. C. Zhang, I. R. Fisher, Z. Hussain, and Z. X. Shen, Science **325**, 178 (2009).

[26] D. X. Qu, Y. S. Hor, J. Xiong, R. J. Cava, and N. P. Ong, Science **329**, 821 (2010).

[27] S. K. Kushwaha, I. Pletikosic, T. Liang, A. Gyenis, S. H. Lapidus, Y. Tian, H. Zhao, K. S. Burch, J. J. Lin, W. D. Wang, H. W. Ji, A. V. Fedorov, A. Yazdani, N. P. Ong, T. Valla, and R. J. Cava, Nat. Commun. **7**, 11456 (2016).

[28] S. K. Kushwaha, Q. D. Gibson, J. Xiong, I. Pletikosic, A. P. Weber, A. V. Fedorov, N. P. Ong, T. Valla, and R. J. Cava, J. Appl. Phys. **115**, 143708 (2014).

[29] See Supplemental Material at XXX for additional experimental (single crystal XRD, powder XRD, EDX and Raman) information.

[30] C. Park, D. Popov, D. Ikuta, C. L. Lin, C. Kenney-Benson, E. Rod, A. Bommannavar, and G. Shen, Rev. Sci. Instrum. **86**, 072205 (2015).

[31] C. Prescher, and V. B. Prakapenka, High Pressure Res. **35**, 223 (2015).

[32] B. A. Hunter,Rietica—AVisualRietveldProgram, International Union of Crystallography Commission on Powder Diffraction Newsletter No. 20 (Summer 1998), http://www.rietica.org.

[33] H. K. Mao, J. Xu, and P. M. Bell, J. Geophys. Res. **91**, 4673 (1986).

[34] J. Xiong, Y. K. Luo, Y. H. Khoo, S. Jia, R. J. Cava, and N. P. Ong, Phys. Rev. B **86**, 045314 (2012).

[35] O. Pavlosiuk, D. Kaczorowski, and P. Wisniewski, Sci. Rep. **5**, 9158 (2015).

[36] H. T. He, G. Wang, T. Zhang, I. K. Sou, G. K. Wong, J. N. Wang, H. Z. Lu, S. Q. Shen, and F. C. Zhang, Phys. Rev. Lett. **106**, 166805 (2011).

[37] H. T. He, B. K. Li, H. C. Liu, X. Guo, Z. Y. Wang, M. H. Xie, and J. N. Wang, Appl. Phys. Lett. **100**, 032105 (2012).

[38] N. R. Werthamer, E. Helfand, and P. C. Hohenberg, Phys. Rev. **147**, 295 (1966).

[39] F. Birch, Phys. Rev. **71**, 809 (1947).

[40] V. Rajaji, P. S. Malavi, S. S. R. K. C. Yamijala, Y. A. Sorb, U. Dutta, S. N. Guin, B. Joseph, S. K. Pati, S. Karmakar, K. Biswas, and C. Narayana, Appl. Phys. Lett. **109**, 171903 (2016).

[41] V. Rajaji, U. Dutta, P. C. Sreeparvathy, S. C. Sarma, Y. A. Sorb, B. Joseph, S. Sahoo, S. C. Peter, V. Kanchana, and C. Narayana, Phys. Rev. B **97**, 085107 (2018).

[42] Y. H. Zhou, X. L. Chen, R. R. Zhang, J. F. Shao, X. F. Wang, C. An, Y. Zhou, C. Y. Park, W. Tong, L. Pi, Z. R. Yang, C. J. Zhang, and Y. H. Zhang, Phys. Rev. B **93**, 144514 (2016).

FIGURES AND CAPTIONS

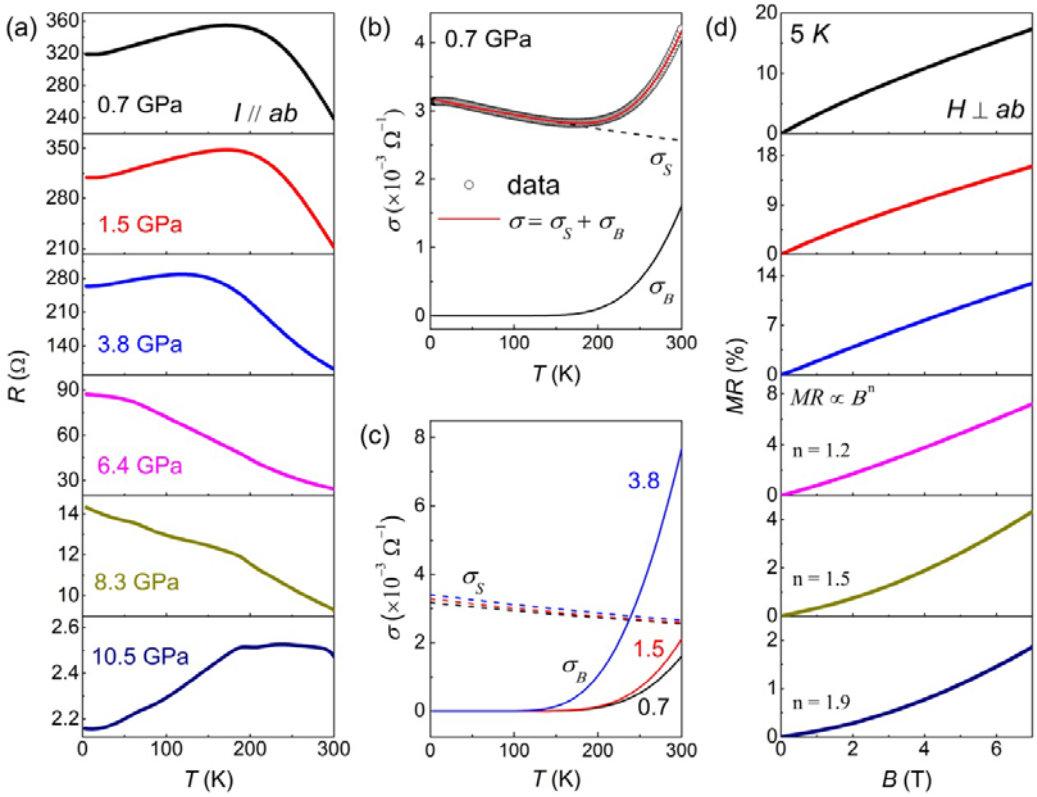

FIG. 1. (Color online) (a) Resistance (R) versus temperature (T) curves in the pressure range of 0.7-10.5 GPa. The current (I) is introduced in the *ab* plane of the single crystal. (b) Temperature dependence of the conductivity at 0.7 GPa fitted by the formula of $\sigma(T)=\sigma_S(T)+\sigma_B(T)$ (red line). More details can be found in the main text. (c) Evolutions of the surface and bulk conductivities with pressures to 3.8 GPa. (d) Magnetoresistance (MR) measured at 5 K and 7 T under pressures to 10.5 GPa.

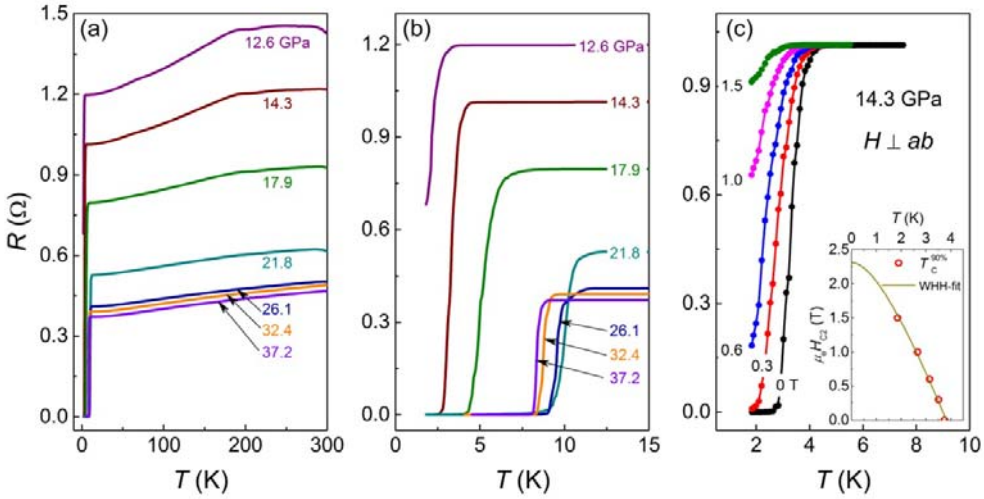

FIG. 2. (Color online) (a) Temperature dependence of the resistance in the pressure range of 12.6~37.2 GPa. (b) An enlarged view of the low temperature resistance, highlighting the superconducting transition. (c) Temperature dependence of the resistance under different magnetic fields up to 1.5 T. The applied pressure is 14.3 GPa. Inset of Figure (c) shows temperature dependence of the upper critical field $\mu_0 H_{C2}$(T). The solid line is the WHH fit to the data and $\mu_0 H_{C2}(0)$ is estimated to be 2.31 T.

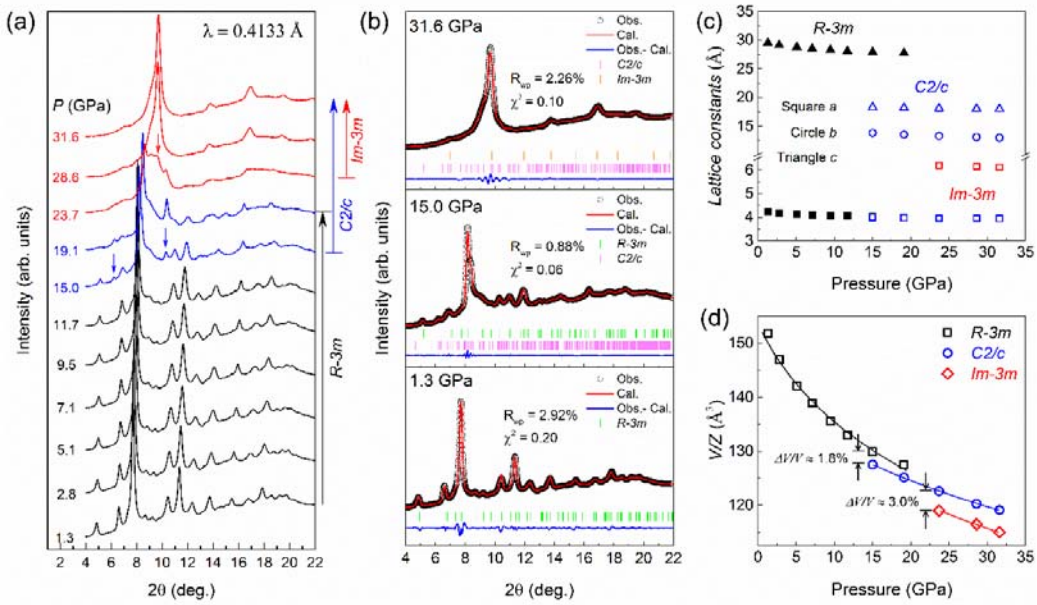

FIG. 3. (Color online) (a) Synchrotron x-ray diffraction patterns of Sn-BSTS at room temperature with pressures up to 31.6 GPa (λ=0.4133 Å). (b) Typical Rietveld refinement results at 1.3 GPa, 15.0 GPa and 31.6 GPa by using the Le Bail method. (c) Lattice parameters as a function of pressure. (d) The unit-cell volume versus pressure. The data was fitted by the third-order Birch-Murnaghan formula.

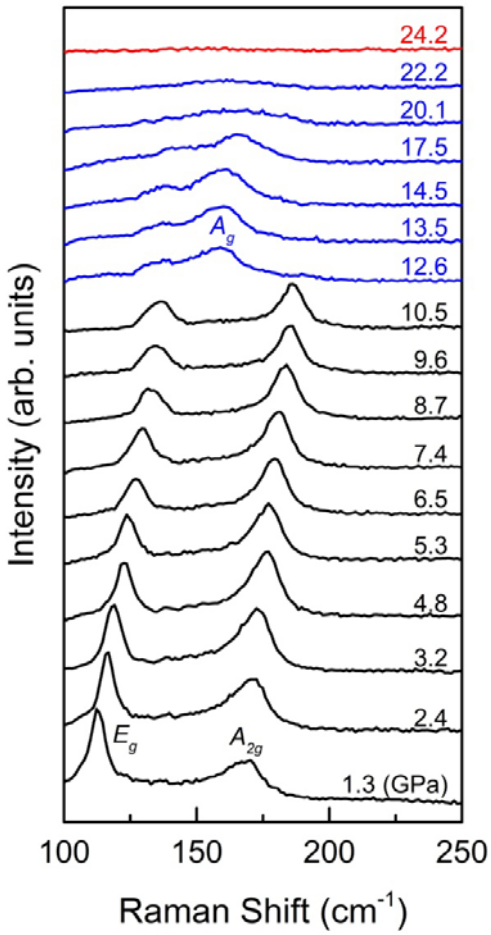

FIG. 4. (Color online) Selected Raman spectra of Sn-BSTS at room temperature with pressures up to 24.2 GPa.

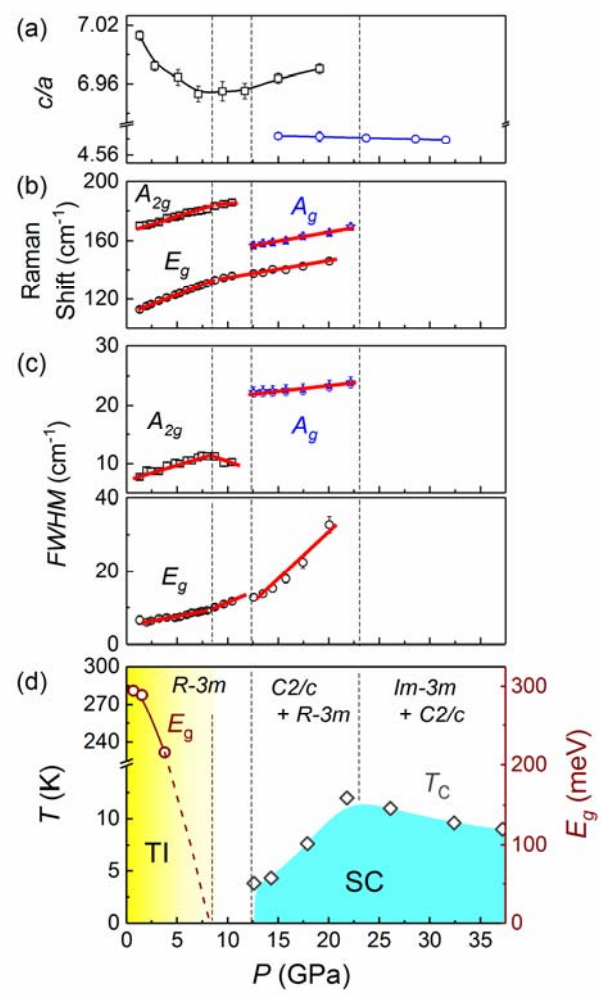

FIG. 5. (Color online) (a) Lattice ratio of *c/a* as a function of pressure. (b) Pressure dependence of Raman frequencies of Sn-BSTS. Solid lines are linear fits to data. (c) Pressure dependence of FWHM of Sn-BSTS. Solid line denotes linear fits to data. (d) Pressure-temperature diagram of Sn-BSTS. The left axis stands for temperature T and the right axis corresponds to the bulk bandgap E_g. "TI" and "SC" denote topological insulators and superconductivity, respectively.